Citation for final published version:

Mil-Martínez, Alejandra M., Vargas, René O., Gómez-López, Aldo, Escandón, Juan P., Martínez-Suástegui, Lorenzo and Phillips, Timothy 2026. Rheo-kinetic predictions using a finitely extensible nonlinear elastic transient network model, Part I: Simple shear flow. Journal of Non-Newtonian Fluid Mechanics 348 , 105566. 10.1016/j.jnnfm.2026.105566

Publishers page: https://doi.org/10.1016/j.jnnfm.2026.105566

Rheo-kinetic Predictions using a Finitely Extensible Nonlinear Elastic Transient Network Model. Part I: Simple Shear Flow

Alejandra Mil-Martínez[1], René O. Vargas[1,4,*], Aldo Gómez-López[2], Juan P. Escandón[1], Lorenzo Martínez-Suástegui[1,3], Timothy N. Phillips[4]

Abstract

This study presents multiscale simulations of complex fluids confined between parallel plates under simple shear flow, employing a finitely extensible nonlinear elastic (FENE) transient network model. The model integrates microscopic kinetic equations for microstructural breaking and recombination processes with macroscopic flow equations, enabling the prediction of nonlinear velocity and stress fluctuations. A hybrid micro–macro numerical framework is developed to capture the coupling between microstructural dynamics and macroscopic rheology. Numerical experiments explore the influence of kinetic rate constants, viscosity ratio, elasticity, extension length, and inertia on flow instabilities. The results reveal that considering viscosity as a function of microstructural kinetics induces fluctuations in the velocity field. These fluctuations occur when the rate of interaction between microstructures reaches a certain value. The fluctuations decrease when the system is dilute or elasticity is increased, and increase for short microstruc-

---

[*] Corresponding author

Email address: `rvargasa@ipn.mx` (René O. Vargas)

[1] ESIME Azcapotzalco, Instituto Politécnico Nacional, Avenida de las Granjas 682, Colonia Santa Catarina, Alcaldía Azcapotzalco, Ciudad de México 02250, Mexico.

[2] Universidad Nacional Autónoma de México, FES Cuautitlán, Departamento de Ingeniería, Sección Mecánica, Av. Teoloyuca Km 2.5, Colonia San Sebastián Xhala, Cuautitlán Izcalli, Estado de México, 54714, Mexico.

[3] Universidad Autónoma de la Ciudad de México, Colegio de Ciencia y Tecnología, Ciudad de México, 09940, Mexico. (sabbatical leave)

[4] School of Mathematics Cardiff University, Senghennydd Road Cardiff CF24 4AG United Kingdom.

Preprint submitted to Journal of Non-Newtonian Fluids Mechanics *February 3, 2026*

tural chain extensions and increasing inertia. These findings establish a direct connection between molecular-scale restructuring and macroscopic flow, thereby contributing to the fundamental understanding of flow instabilities and providing guidance for modelling complex fluids.

Keywords: Fluctuations, FENE transient network, Multiscale model

---

1. Introduction

Complex fluids can be described as fluids with internal microstructures, the evolution of which influences the macroscopic dynamics of the material, including its rheology [1]. Examples of complex fluids are food, biological materials, and plastic coatings [2]. The internal microstructure of a complex fluid is reorganized under flow, which in turn modifies the flow field, resulting in highly nonlinear flow properties [3] and phenomena such as shear banding [4]. Network models are characterised by breaking and recombination processes that determine the degree of entanglement of polymer chains and how they evolve in response to flow and energy changes. Classical transient network models consider the creation of microstates as a thermal activation process, while flow breaks the network [5–7]. Rincón et al. [8] proposed the formation of a transient network through five microstates, using the moments of the distribution function to calculate the rheological functions [9]. Manero et al. [10] presented a simplified expression of the kinetics of the microstates, leading to a global scheme instead of a detailed kinetics of the evolution of each microstate. García-Sandoval et al. [11] analysed the kinetics of the entanglement–disentanglement process of complex fluids coupled to a rheological constitutive equation of state within an irreversible thermodynamics framework. Quintero F. et al. [12] formulated a mesoscale stochastic rupture/reform model in which single weights can join to form double weights and double weights can separate to form single weights. The topology was tracked in the simulation and finite extensible non-linear elastic (FENE) springs were taken into account. In the classical FENE model [13], the nonlinear dumbbell possesses a constant maximum extensibility. However, in the transient network model proposed by Rincón et al. [8], the maximum extensibility is not a constant, but a variable resulting from a kinetic process. Ferrer et al. [14] coupled the FENE model with the transient network model to describe the behaviour of a complex fluid under simple shear flow. Constitutive equations based on microstructural theories that are simple enough to solve a complex flow include the Vasquez-Cook-McKinley (VCM) [15] and the simplified living Rolie-Poly (RP) [16] models. Germann et al. [17] reviewed the VCM model from a non-equilibrium thermodynamic point of view. To describe micellar breakage and reformation, they extended the non-equilibrium mass action treatment of chemical reaction kinetics to multicomponent systems with an internal viscoelastic structure. Adams et al. [18] incorporated microscopic reversibility into the VCM model by extending an ensemble-averaged bead-spring phase-space model to include reversible scission of two-spring chains. This model offered the prospect of including additional physics and the ability to test the accuracy of closure approximations by parallel Brownian dynamics simulations. Lerouge and Olmsted [19] proposed that to physically model shear banding, the stress tensor must incorporate stresses due to microstructural quantities, such as molecular or segmental orientation, micellar length, and concentration fields in polymeric fluids. In this study, we present a multiscale modeling approach for complex fluids confined between parallel plates, employing a FENE transient network model [20, 21]. The model incorporates a microstructural kinetic mechanism of bond breaking and recombination, which induces nonlinearities in the velocity field. We analyse the influence of kinetic rate constants, viscosity ratio, elasticity, and inertia on the overall flow behaviour.

The paper is organised as follows. The macroscopic and microscopic elements of the mathematical model are presented in Section 2. In Section 3 the dimensionless form of the governing equations is derived. The discretization of the computational domain and the governing equations are described in Sections 4 and 5, respectively. The numerical predictions for a range of model parameters are presented in Section 6. Finally, concluding remarks are given in Section 7.

2. Mathematical Model

In this work, a hybrid micro-macro model is used as the basis for numerical predictions since the approach provides greater flexibility in the modelling of polymeric fluids. Not all kinetic theory models have closed-form macroscopic equivalents and the micro-macro approach circumvents the need to implement closure approximations that are not universally accurate. We assume that the fluid is incompressible.

2.1. Macroscopic Equations

The governing equations are the conservation equations of mass

$$\nabla \cdot \mathbf{v} = 0, \tag{1}$$

and momentum

$$\rho \left(\frac{\partial \mathbf{v}}{\partial t} + \mathbf{v} \cdot \nabla \mathbf{v} \right) = -\nabla p + \nabla \cdot \boldsymbol{\sigma}, \tag{2}$$

where $\mathbf{v}$ is the velocity, ρ is the density, p is the pressure and $\boldsymbol{\sigma}$ is the extra-stress tensor. The extra-stress tensor $\boldsymbol{\sigma}$ is decomposed into solvent and polymeric contributions, $\boldsymbol{\sigma}^{\mathrm{s}}$ and $\boldsymbol{\sigma}^{\mathrm{p}}$, respectively, where $\boldsymbol{\sigma} = \boldsymbol{\sigma}^{\mathrm{s}} + \boldsymbol{\sigma}^{\mathrm{p}}$. The solvent contribution is given by $\boldsymbol{\sigma}^{\mathrm{s}} = 2\eta_{\mathrm{s}}\boldsymbol{d}$, where η_{s} is the solvent viscosity and

$$\boldsymbol{d} = \frac{1}{2} \left(\nabla \mathbf{v} + (\nabla \mathbf{v})^T \right), \tag{3}$$

is the rate-of-strain tensor. With this decomposition, the momentum equation can be written in the form

$$\rho \frac{D\mathbf{v}}{Dt} = -\nabla p + 2\nabla \cdot (\eta_s \boldsymbol{d}) + \nabla \cdot \boldsymbol{\sigma}^{\mathrm{p}}. \tag{4}$$

The polymeric contribution to the stress tensor is traditionally calculated using a differential or integral constitutive equation. However, there are models of kinetic theory that are able to provide an accurate representation of polymeric fluids, but that do not possess an equivalent closed-form constitutive equation. For this reason, in this paper the polymeric contribution to the stress is evaluated by means of a microscopic description of polymer dynamics.

2.2. Microscopic Equations

Consider an elastic dumbbell comprising two identical beads and a connecting elastic spring immersed in a Newtonian solvent. Suppose that the configuration of the dumbbell is represented by the end-to-end vector $\mathbf{Q}$, which provides information about the stretch and orientation of the dumbbell. The equation of motion for the beads can be derived by considering the following forces: the forces due to Brownian motion, the elastic spring force, and the viscous drag force on the beads. This is the starting point for the derivation of the Fokker-Planck equation, the details of which can be found in Öttinger

[22], for example. For the FENE dumbbell model, the Fokker-Planck equation is

$$\frac{\partial}{\partial t}\psi = -\frac{\partial}{\partial \mathbf{Q}}\left\{\left(\boldsymbol{\kappa}(t)\cdot\mathbf{Q} - \frac{2}{\varsigma}\mathbf{f}(\mathbf{Q})\right)\psi\right\} + \frac{2k_bT}{\varsigma}\frac{\partial}{\partial \mathbf{Q}}\frac{\partial}{\partial \mathbf{Q}}\psi, \tag{5}$$

where ψ is the configuration of the probability density function (pdf) and $\psi(\mathbf{Q}, \mathbf{x}, t)d\mathbf{Q}$ represents the probability of finding a dumbbell with configuration in the range $\mathbf{Q}$ to $\mathbf{Q} + d\mathbf{Q}$ in $(\mathbf{x}, t)$, $\boldsymbol{\kappa}(t)$ is the velocity gradient, ς is the friction coefficient, k_b is Boltzmann's constant, T is the absolute temperature, and $\mathbf{f}$ represents the spring force which, for FENE dumbells, is given by

$$\mathbf{f}(\mathbf{Q}) = \frac{H\mathbf{Q}}{1-(\mathbf{Q}/Q_{\max})^2}, \tag{6}$$

where H is the spring constant and $Q_{\max}$ is the maximum spring extension. The high-dimensional nature of the Fokker-Planck equation means that it is expensive to solve computationally. However, one can use the equivalence between Eq. (5) and the stochastic differential equation.

$$d\mathbf{Q}(t) = \left(\boldsymbol{\kappa}(t)\cdot\mathbf{Q} - \frac{2}{\varsigma}\mathbf{f}(\mathbf{Q})\right)dt + \sqrt{\frac{4k_bT}{\varsigma}}d\boldsymbol{\Phi}(t), \tag{7}$$

as the basis for deriving computationally tractable numerical schemes. In this equation $\boldsymbol{\Phi}(t)$ is a multi-dimensional Wiener process, (see [22–24], for details). It is possible to establish a relation between the material constants at the microscopic and macroscopic levels: $\lambda = \varsigma/4H$ and $\eta_{\mathrm{p}} = nk_bT\lambda$, where λ, η_{p}, n are the relaxation time, polymeric viscosity, and the number of dumbbells per unit of volume, respectively. Every dumbbell is characterized by λ and $Q_{\max}$. Once the configuration is determined, $\boldsymbol{\sigma}^{\mathrm{p}}$ is evaluated using the Kramers expression [9, 23]:

$$\boldsymbol{\sigma}^{\mathrm{p}} = -nk_bT\mathbf{I} + n\mathbf{Q}\mathbf{f}(\mathbf{Q}) = \frac{\eta_{\mathrm{p}}}{\lambda}(-\mathbf{I} + \ \mathbf{Q}\mathbf{f}(\mathbf{Q})). \tag{8}$$

2.3. Transient Network Model

The FENE dumbbell model is a coarse level of description of the polymer conformation of a polymer chain. For a dilute polymer solution, the interactions between polymer chains are generally not considered in this model. However, many chain molecules tend to become entangled or disentangled as

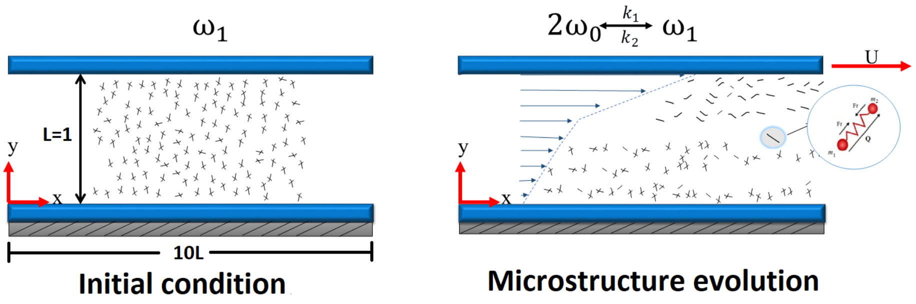

Figure 1: Complex fluid confined between parallel plates. Left: initially a microstate (ω_1) is present in a Newtonian solvent. Right: subsequently the flow separates into bands comprising two different microstates under simple shear flow.

Microstate	Number of nodes	Number of segments	Number of chains	l_i
ω_0	0	1	1	1
ω_1	1	4	2	1/2

Table 1: Microstate properties.

a result of flow or energy considerations. These processes produce time varying local changes in properties like maximum chain length, elastic constant and relaxation time. In the following we describe how the FENE model can be modified to account for these interactions utilizing a transient network model.

In the dilute regime, it is possible to consider a small number of interactions and small or negligible changes for every dumbbell. As the concentration increases, those changes are not negligible. These changes in behaviour can be modelled by defining some characteristic states termed microstates (see Fig. 1) that are defined by the number of chain segments and the number of nodes required to produce it [8]. Within this framework, there are different ways to determine what constitutes a microstate. In this paper only two microstates ω_i, $i = 0, 1$, are considered. For details of the full model, the reader is referred to Gómez-López et al. [25]. A chain arrangement is defined and identified as shown in Table 1, where l_i represents the fraction of maximum extension length for each microstate [8, 14]. As we have already mentioned, the formation and recombination of microstates depends on the energy of the system used to form or break a node, by viscous dissipation or in the equilibrium state. Based on this information, a kinetic scheme analogous to that of a chemical reaction is proposed, whereby physical interactions between chains create and destroy microstates, which depend on the number of chain segments and the number of nodes or interaction points. Creation is a function of free energy, while rupture is a function of viscous dissipation, the latter being a process in which the chains untangle and align themselves in the direction of the main flow:

$$2\omega_0 \underset{k_1^{\mathrm{B}}\boldsymbol{\sigma} : \dot{\boldsymbol{\gamma}}}{\overset{k_1^{\mathrm{A}} \exp\left(-\frac{E_0}{k_b T}\right)}{\rightleftarrows}} \omega_1, \tag{9}$$

where k_1^{A}, k_1^{B} represent the formation and breakage constants for each microstate, respectively, and E_0 is the energy required to create a node. If we consider the formation and recombination constants to be proportional to the number of nodes to create every microstate, it is possible to consider k^A and k^B as the formation and recombination kinetic constants to establish the following system of ordinary differential equations:

$$\frac{DC_0}{Dt} = 2k^B\, \boldsymbol{\sigma} : \dot{\boldsymbol{\gamma}} C_1 - k^A C_0^2 + D_m \nabla^2 C_0, \tag{10}$$

$$\frac{DC_1}{Dt} = -k^B\, \boldsymbol{\sigma} : \dot{\boldsymbol{\gamma}} C_1 + \frac{1}{2} k^A C_0^2 + D_m \nabla^2 C_1, \tag{11}$$

where $\frac{D}{Dt}$ is the material derivative, D_m is the diffusion coefficient, C_0 and C_1 are the concentrations of microstructures ω_0 and ω_1, respectively. Each microstate ω_i defines a microstructure in a region of space, which behaves as a dumbbell with its own properties: partial viscosity fraction η_{pi}, relaxation time τ_i and maximum extension length b_i, as shown in Table 2. Under these assumptions, the stress produced by each microstructure is obtained by the Kramers expression:

$$\boldsymbol{\sigma}^{\mathrm{p}} = \sum_{i=0}^{1} -C_i k_b T \mathbf{I} + C_i \left\langle \mathbf{Q}_i \mathbf{f}_i(\mathbf{Q}_i) \right\rangle = \sum_{i=0}^{1} \frac{\eta_{pi}}{\lambda_i} \left(-\mathbf{I} + \frac{1}{k_b T} \left\langle \mathbf{Q}_i \mathbf{f}_i(\mathbf{Q}_i) \right\rangle \right), \tag{12}$$

where $\eta_p = \sum_{i=0}^{1} \eta_{pi} = C_i k_b T \lambda_i$, $\mathbf{f}_i$, and λ_i are the viscosity, spring force, and relaxation time associated with the microstate ω_i, respectively. The angular brackets denote the ensemble average over the configuration space.

2.4. Dimensionless Equations

Let L, U, and C_c denote characteristic length, velocity, and concentration scales, respectively. Dimensionless variables are defined as follows:

$$\mathbf{x}^* = \frac{\mathbf{x}}{L},\ \ \mathbf{v}^* = \frac{\mathbf{v}}{U},\ \ t^* = \frac{t}{L/U},\ \ C^* = \frac{C}{C_c},\ \ p^* = \frac{p}{\eta_0 U/L},\ \boldsymbol{\sigma}^{\mathrm{p}*} = \frac{\boldsymbol{\sigma}^{\mathrm{p}}}{\eta_0 U/L}, \tag{13}$$

where η_0 denotes the zero shear viscosity defined by $\eta_0 = \eta_{\mathrm{s}} + \eta_{\mathrm{p}}$ in the initial state. The dimensionless macroscopic equations are then

$$\nabla \cdot \mathbf{v}^* = 0, \tag{14}$$

$$\mathrm{Re}\,\frac{D\mathbf{v}^*}{Dt^*} = -\nabla^* p + \beta \nabla^{*2}\mathbf{v}^* + \nabla^*\beta \cdot \nabla^*\mathbf{v}^* + \nabla^* \cdot \boldsymbol{\sigma}^{\mathrm{p}*}, \tag{15}$$

where $\mathrm{Re} = \rho U L/\eta_0$ is the Reynolds number and $\beta = \eta_{\mathrm{s}}/\eta_0$ is the viscosity ratio. The end-to-end vector $\mathbf{Q}$ is dimensionless using $\sqrt{k_b T/H}$ so that the dimensionless stochastic differential equation (7) becomes

$$d\mathbf{Q}_i^* = \left(\boldsymbol{\kappa}^* \cdot \mathbf{Q}_i^* - \frac{1}{2\lambda_H}\mathbf{f}(\mathbf{Q}_i^*)\right) dt + \frac{1}{\sqrt{\lambda_H}} d\boldsymbol{\Phi}, \tag{16}$$

where $\lambda_H = \xi/(4H)$ is the relaxation time and the dimensionless force is

$$\mathbf{f}(\mathbf{Q}^*) = \frac{\mathbf{Q}^*}{1 - (\mathbf{Q}^*/\mathbf{Q}_{\max})^2}.$$

We assume that the viscosity of the microstate ω_0 is the solvent viscosity, $\eta_{\mathrm{s}} = \eta_{\mathrm{p}0}$. Polymeric stress is evaluated using the Kramers expression:

$$\begin{aligned} \boldsymbol{\sigma}^{\mathrm{p}*} \ \ &= \ \ \frac{\beta}{\tau_0 \mathrm{Wi}} \alpha_0 \left(\langle \mathbf{Q}_0^* \otimes \mathbf{f}_0(\mathbf{Q}_0^*) \rangle - \mathbf{I} \right) \\ &\quad + \frac{(1-\beta)}{\tau_1 \mathrm{Wi}} \alpha_1 \left(\langle \mathbf{Q}_1^* \otimes \mathbf{f}_1(\mathbf{Q}_1^*) \rangle - \mathbf{I} \right), \end{aligned} \tag{17}$$

where $\mathrm{Wi} = \lambda_H U/L$ is the Weissenberg number, $\tau_i = \lambda_i/\lambda_H$ is the relaxation time of the ith microstructure, $\alpha_i = \frac{b_i+d+2}{b_i}$, where d is the spatial dimension of the problem, and $b_i = b l_i^2$ is the dimensionless maximum extension length of the ith microstructure ω_i, where $b = HQ_{max}^2/k_bT$. The dimensionless form of the stochastic differential equations for each microstructure is:

$$
\begin{aligned}
d\mathbf{Q}_0^* &= \left(\boldsymbol{\kappa}^* \cdot \mathbf{Q}_0^* - \frac{1}{2\tau_0 \mathrm{Wi}} \mathbf{f}_0(\mathbf{Q}_0^*) - k_1^* \mathbf{Q}_0^* + 2k_2^* \mathbf{Q}_1^*\right) dt^* \\
&\quad + \sqrt{\frac{1}{\tau_0 \mathrm{Wi}}} d\mathbf{W},
\end{aligned} \tag{18}
$$

$$
\begin{aligned}
d\mathbf{Q}_1^* &= \left(\boldsymbol{\kappa}^* \cdot \mathbf{Q}_0^* - \frac{1}{2\tau_1 \mathrm{Wi}} \mathbf{f}_1(\mathbf{Q}_1^*) + \frac{k_1^*}{2} \mathbf{Q}_0^* - k_2^* \mathbf{Q}_1^*\right) dt^* \\
&\quad + \sqrt{\frac{1}{\tau_1 \mathrm{Wi}}} d\mathbf{W},
\end{aligned} \tag{19}
$$

where $\mathbf{W}$ represents the dimensionless Wiener process, that is, Gaussian processes with zero mean and covariance $\langle W(t)W(t)\rangle = \min(t,t)\mathbf{I}$ [22–24]. Equations (18) and (19) are similar to Eq. (16) except that additional terms have been included to account for the kinetic process (breakup/recombination).

Microstructure	τ_i	l_i
ω_0	1	1
ω_1	1/2	1/2

Table 2: Microstructure coefficients.

For the concentrations, the dimensionless equations are in term $A = \frac{K^A L C_c}{U}$, which describes the ratio of the reaction rate to the advective transport rate and $B = \frac{K^B \eta_o U}{L C_c}$, which is the ratio of the dissipative process rate to the advective transport rate as follows

$$
\frac{DC_0^*}{Dt^*} = B\,\boldsymbol{\sigma}^* : \dot{\boldsymbol{\gamma}}^* C_1^* - A\, {C^*}_0^2 + \frac{1}{Pe} \nabla^{*2} C_0^*, \tag{20}
$$

$$
\frac{DC_1^*}{Dt^*} = -B\,\boldsymbol{\sigma}^* : \dot{\boldsymbol{\gamma}}^* C_1^* + A\, {C^*}_0^2 + \frac{1}{Pe} \nabla^{*2} C_1^*, \tag{21}
$$

where $Pe = \frac{UL}{D}$ is the Peclet number, which relates the ratio of advective transport rate to diffusion transport rate. In order to simplify the notation, the symbol $*$ is omitted from here onwards.

3. Computational Model

3.1. Computational Domain

Consider the start-up of a simple shear flow in a channel. The channel contains a complex fluid that is initially at rest. At time $t = 0$, the top wall moves instantaneously with axial velocity $u = 1$, generating flow in the channel. The bottom wall remains stationary. At the entrance and exit of the channel, we impose $u_x = 0$. In this paper, the evolution of the resulting flow is studied for a range of material and flow parameters.

Consider the computational domain $[0, 10] \times [0, 1]$. The governing equations are discretized using a finite difference scheme, and three meshes are considered for the mesh refinement study: $M_1 - M_3$ (40×40), (50×50) and (60×60), respectively. The equations are solved for $t \in [0, t_{max}]$ where $t_{max} = 100$ using a constant time step of $\Delta t = 10^{-3}$ and the M_3 mesh for all simulations [14, 26].

3.2. Numerical Scheme

The numerical scheme is based on a decoupled approach in which the governing equations are solved in three stages at each time step.

3.2.1. Stage 1: Macroscopic Equations

In the macroscopic stage, we assume knowledge of the polymeric contribution to the extra-stress tensor of the previous time step, $\boldsymbol{\sigma}^{\mathrm{p}}$. The velocity at the new time level is then obtained by solving the following semi-discrete problem.

$$\begin{aligned} \nabla \cdot \mathbf{v}^{n+1} &= 0, & (22) \\ \frac{\mathrm{Re}}{\Delta t}\left(\mathbf{v}^{n+1} - \tilde{\mathbf{v}}^{n+1}\right) &= -\nabla p^{n+1} + \beta \nabla^2 \mathbf{v}^{n+1} + \nabla \beta \cdot \nabla \mathbf{v}^{n+1} \\ &\quad + \nabla \cdot \boldsymbol{\sigma}^{\mathrm{p}n}. & (23) \end{aligned}$$

This is an implicit treatment of the conservation equations where $\tilde{\mathbf{v}}^{n+1}$ is the solution of the following pure convection problem at time $t = t^{n+1}$:

$$\frac{\partial \tilde{\mathbf{v}}}{\partial t} = -\mathbf{v}^n \cdot \nabla \tilde{\mathbf{v}}, \; t \in [t^n, t^{n+1}], \;\; \tilde{\mathbf{v}}(\mathbf{x}, t^n) = \mathbf{v}(\mathbf{x}, t^n). \tag{24}$$

This equation is solved over the interval $[t^n, t^{n+1}]$. The conservation equations (22) - (23) are solved iteratively using the Alternating Direction Implicit (ADI) method [26].

3.2.2. Stage 2: Concentration Equations

The concentration equations (20) and (21) are solved using an explicit method in which the viscous dissipation term is evaluated at time $t = t_n$.

3.2.3. Stage 3: Microscopic Equations

Hulsen et al. [27] developed the Brownian configuration fields method (BCFM) to overcome the problem of having to track individual particle trajectories Subsequent implementations of BCFM within a spectral element context can be found in Smith and Phillips [28] and Vargas et al. [29]. The method is based on the evolution of a number of continuous configuration fields by combining dumbbell connectors with same initial configuration and subject to the same random forces throughout the flow to form a configuration field. An additional term needs to be included in the stochastic differential equations (18) and (19) to account for the convection of the configuration field by the flow (see Lozinski et al. [30]). The modified equation is

$$\begin{aligned} d\mathbf{Q}_m(t) &= \left(-\mathbf{v}\cdot\nabla\mathbf{Q}_m + \boldsymbol{\kappa}(t)\cdot\mathbf{Q}_m - \frac{1}{2\lambda}\mathbf{f}(\mathbf{Q}_m) + R_k\right)dt \\ &\quad + \sqrt{\frac{1}{\lambda}}\,d\mathbf{\Phi}_m(t), \quad m = 1,\ldots,N_f, \end{aligned} \tag{25}$$

where R_k is the kinetic term and N_f is the number of configuration fields. The main idea underlying BCFM is the assumption that the same initial ensemble of dumbbells is located at every spatial discretization point instead of independent ensembles, which enables the same sequence of random numbers to be used to build the trajectories of many groups of dumbbells.

As the second moment of the Wiener process is of the order $O(t)$ and using the properties of $\mathbf{\Phi}(t)$ described previously, Eq. (25) becomes

$$\begin{aligned} d\mathbf{Q}_m(t) &= \left(-\mathbf{v}\cdot\nabla\mathbf{Q}_m + \boldsymbol{\kappa}(t)\cdot\mathbf{Q}_m - \frac{1}{2\lambda}\mathbf{f}(\mathbf{Q}_m) + R_k\right)dt \\ &\quad + \mathbf{\Phi}_m\sqrt{\frac{dt}{\lambda}}. \end{aligned} \tag{26}$$

A set of conformation vectors that experience the same deformation history is generated at each discretization point in space and time, with different stochastic processes. Polymeric stress $\boldsymbol{\sigma}^{\mathrm{p}}$ can be determined from the conformation vectors as follows:

$$\boldsymbol{\sigma}^{\mathrm{p}}(\mathbf{X},t) = \frac{\eta_{\mathrm{p}}}{\lambda}\Big(-\mathbf{I} + \frac{1}{N_f}\Big(\sum_{m=1}^{N_f} \mathbf{Q}_m(\mathbf{X},t)\mathbf{Q}_m(\mathbf{X},t)\Big)\Big). \tag{27}$$

Initially, the fluid is stationary so that $\boldsymbol{\sigma}^{\mathrm{p}} = \mathbf{0}$ at $t = 0$ and at every spatial discretization point the conformation fields must satisfy:

$$\lim_{N_f\to\infty} \sum_{m=1}^{N_f} \mathbf{Q}_m(\mathbf{X},t_0)\mathbf{Q}_m(\mathbf{X},t_0) = \langle \mathbf{Q}\mathbf{Q}\rangle = \mathbf{I}. \tag{28}$$

Since the statistical error is proportional to $1/\sqrt{N_f}$ as $N_f \to \infty$, then the numerical convergence is of order $O(1/\sqrt{N_f})$ according to the central limit theorem. Eq. (26) can be generalized to be applicable for each microstate:

$$\begin{aligned} d\mathbf{Q}_{ij}(t) &= \left(-\mathbf{v}\cdot\nabla\mathbf{Q}_{ij} + \boldsymbol{\kappa}(t)\cdot\mathbf{Q}_{ij} - \frac{1}{2\lambda_i}\mathbf{f}(\mathbf{Q}_{ij}) + R_k\right)dt \\ &\quad +\boldsymbol{\Phi}_{ij}\sqrt{\frac{dt}{\lambda}}_i,\ i = 0,1,\ j = 1,\ldots,N_f, \end{aligned} \tag{29}$$

in which case the polymeric contribution to the extra-stress tensor at the new time level t^{n+1} is then calculated using the following:

$$\begin{aligned} (\boldsymbol{\sigma}^{\mathrm{p}})^{n+1} &= \alpha_0\frac{\beta}{\tau_0\mathrm{Wi}}\left(-\mathbf{I} + \frac{1}{N_f}\sum_{j=1}^{N_f}\langle \mathbf{Q}_{0j}\otimes\mathbf{f}_0(\mathbf{Q}_{0j})\rangle\right) \\ &\quad +\alpha_1\frac{(1-\beta)}{\tau_1\mathrm{Wi}}\left(-\mathbf{I} + \frac{1}{N_f}\sum_{j=1}^{N_f}\langle \mathbf{Q}_{1j}\otimes\mathbf{f}_1(\mathbf{Q}_{1j})\rangle\right), \end{aligned} \tag{30}$$

where N_f is the number of trajectories. The temporal discretization of the evolution equation for the configuration fields in Eq. (29) is performed using a second-order predictor-corrector scheme, which is based on a forward Euler predictor and trapezoidal corrector:

$$\begin{aligned} \bar{\mathbf{Q}}_{ij}^{n+1} &= \mathbf{Q}_{ij}^n + \Big(-\mathbf{v}^n\cdot\nabla\mathbf{Q}_{ij}^n + \kappa^n\mathbf{Q}_{ij}^n - \frac{1}{2\tau_i\mathrm{Wi}}\mathbf{f}(\mathbf{Q}_{ij}^n) + R_k^n\Big)\Delta t \\ &\quad +\sqrt{\frac{1}{\tau_i\mathrm{Wi}}}d\mathbf{W}_j^n \end{aligned} \tag{31}$$

$$\begin{aligned}\mathbf{Q}_{ij}^{n+1} + \frac{\Delta t}{4\tau_i \mathrm{Wi}} \mathbf{f}(\mathbf{Q}_{ij}^{n+1}) \quad = \quad & \mathbf{Q}_{ij} - \frac{1}{2}\Big(\mathbf{v}^{n+1} \cdot \bar{\mathbf{Q}}_{ij}^{n+1} + \mathbf{v}^{n} \cdot \mathbf{Q}_{ij}^{n}\Big)\Delta t \\ & + \frac{1}{2}\Big(\kappa^{n+1}\bar{\mathbf{Q}}_{ij}^{n+1} + \kappa^{n}\mathbf{Q}_{ij}^{n}\Big)\Delta t \\ & - \frac{\Delta t}{4\tau_i \mathrm{Wi}} \mathbf{f}(\mathbf{Q}_{ij}^{n}) + \frac{1}{2}(R_k^{n+1} + R_k^{n})\Delta t \\ & + \sqrt{\frac{1}{\tau_i \mathrm{Wi}}} d\mathbf{W}_j^{n}. \end{aligned} \tag{32}$$

The right-hand side of Eq. (32) gives the orientation of the conformation vector $\mathbf{Q}_{ij}^{n+1}$, with an arbitrary length. In order to obtain the length of $\mathbf{Q}_{ij}^{n+1}$, Eq. (32) is expressed as

$$\Big[1 + \frac{1}{4\tau_i \mathrm{Wi}} \frac{\Delta t}{[1 - x^2/b_i]}\Big] x = \theta, \tag{33}$$

or

$$g(x) := x^3 - \theta x^2 - \Big(1 + \frac{1}{4\tau_i \mathrm{Wi}}\Big) b_i x + \theta b_i = 0, \tag{34}$$

where θ is the right-hand side of Eq. (32) and $x = |\mathbf{Q}_{ij}^{n+1}|$. Öttinger [22] has shown that there exists a unique solution of this cubic equation in the interval $[0, \sqrt{b_i}]$, meaning there is precisely one physically admissible solution. This scheme circumvents difficulties that may arise using other temporal schemes in which unphysical extensions can be generated during the iterative process. A flow chart of this micro-macro algorithm is shown in Fig. 2.

3.2.4. Summary of the calculation procedure

In the first stage, the macroscopic equations are solved. Given the stress tensor from the previous time step, the velocity at the new time step is determined by solving the conservation equations (22)-(24). In the second stage, the evolution equations (20)-(21) of the microstate concentrations are solved using an explicit method. In the final stage, the microscopic equations are solved. Given the velocity field determined in the first stage, the stochastic PDEs are solved for the Brownian configuration fields Eqs. (31)-(34). At the end of each time step, the polymeric stress tensor is updated using the Kramers expression Eq. (30) before moving on to the next time step. In this work, multiscale modelling of complex fluids confined between parallel plates is presented using a FENE-transient network model. The effect of kinetic rate constants (A and B), viscosity ratio β, maximum extension length b,

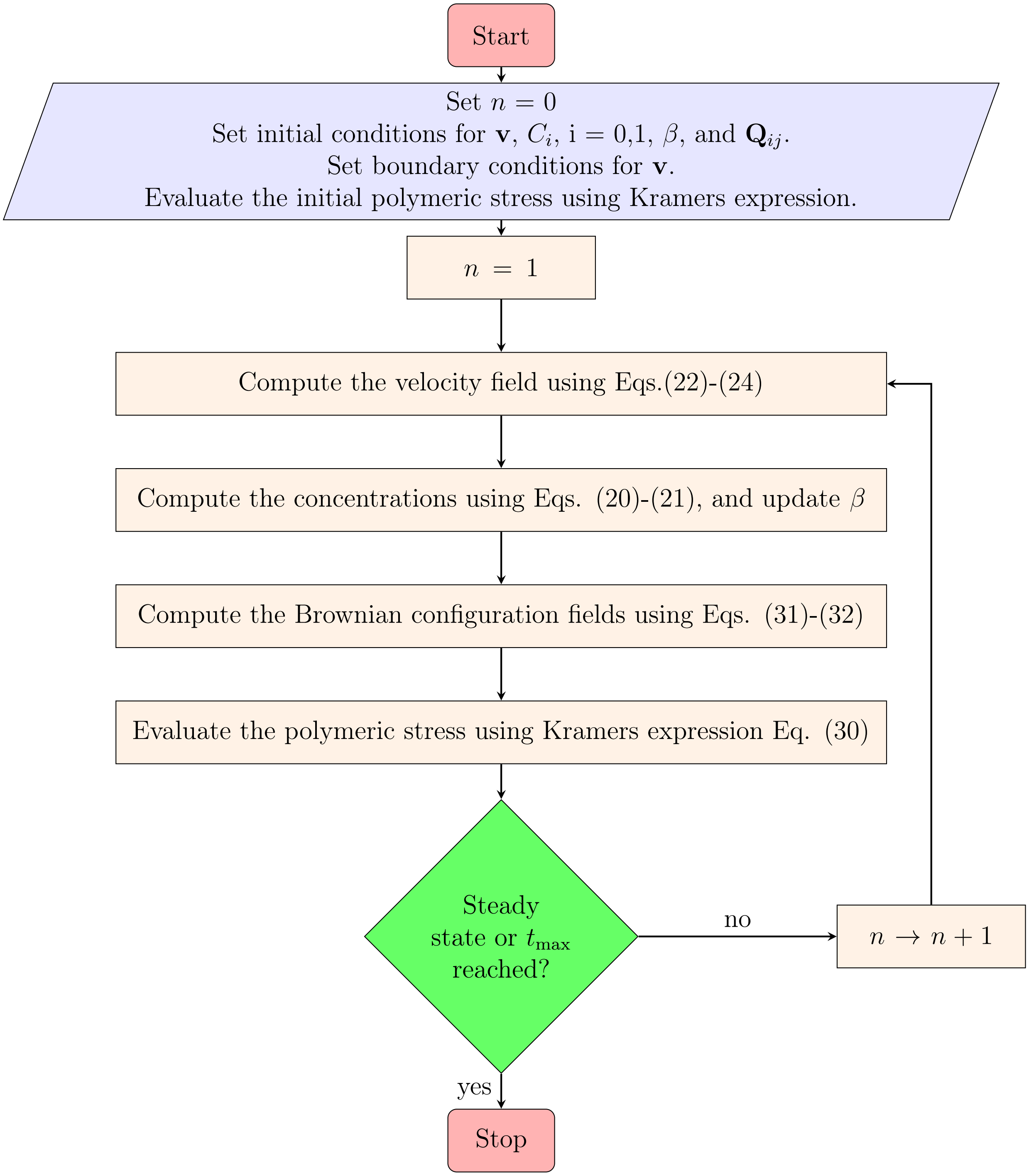

Figure 2: Flow chart for the micro-macro numerical algorithm.

elasticity Wi and inertia Re on the velocity, stress and concentration fields is investigated and analysed.

4. Numerical Results

In this section, numerical solutions for the start-up of a simple shear flow of complex fluids using the FENE transient network model are presented. All numerical results were generated using the decoupled micro-macro numerical scheme shown in Fig. 2 using a Fortran code developed by the authors [14, 20]. The transient network model developed by Rincón et al. [8] and improved by Ferrer et al. [14] and Vargas et al. [20] was incorporated into this numerical code. In a previous paper [20], the code was validated by comparing macroscopic simulations using the Oldroyd B model with a micro-macro approach for Hookean dumbbells. The purpose of the present numerical study is to determine the range of parameters that generate fluctuations in the velocity field for a simple shear flow.

4.1. FENE Transient Network Model

In the first simulation, a transient network that initially comprises only the microstate ω_1 immersed in a Newtonian solvent is considered (see Fig. 1). The values of the other parameters are $\mathrm{Wi} = 1$, $\beta(x, y, t = t_0) = 1/10$, $A = 1$, $B = 1$, $b = 50$. A comparison of axial velocity and shear stress as a function of time for two Reynolds numbers is performed using the three different meshes defined in Section 3.1. Figs. 3(a) and 3(b) present a mesh convergence study of the evolution of axial velocity and shear stress at $(x, y) = (5, 0.75)$ for $\mathrm{Re} = 0.1$ and $\mathrm{Re} = 1$, respectively. Excellent spatial convergence is obtained across all meshes. Based on these results, all subsequent simulations are performed using the mesh M_3. Figure 4 shows the effect of the number of Brownian fields N_f on the average concentrations, velocity, and stress. In the case of concentrations and velocity, the convergence behaviour is excellent. There are differences in the case of stress but these are of the same order and due to the stochastic nature of this component of the simulation. For the following simulations, we will use $N_f = 2000$. Fig. 5 shows the evolution of the averaged microstate concentrations over the entire computational domain, as well as the axial velocity component, u, and the shear stress, σ_{xy}, at $(x, y) = (5, 0.75)$, and the distribution of the microstate concentration ω_1 (contours) and velocity (vectors) at a number of instances at dimensionless times ($t = 0.005, 0.1, 0.3, 0.5, 1.0, 5.0$). Fig. 5(a) shows that initially the microstates ω_1 and ω_0 are broken and recombined, respectively. After time $t \approx 0.7$, the concentration of ω_0 exceeds that of ω_1 before both microstates reach their equilibrium concentrations. Fig. 5(b) shows the evolution of the axial velocity component at $(x, y) = (5, 0.75)$. A typical velocity overshoot of start-up flows of viscoelastic fluids is present within the first two dimensionless time units before a steady-state solution is reached. Fig. 5(c) shows a similar plot for the shear stress. Since the stress is determined using a stochastic technique, noise is to be expected in its temporal development. Fig. 5(d) shows the evolution of the concentration distribution ω_1 and how it develops to reach an equilibrium concentration. The velocity vectors are superimposed on this figure in order to show the transient development toward the final steady state, with the expected linear profile. Adams et al. [18] compared the predictions of the VCM model, which treats wormlike micelles as Hookean dumbbells that break at half-length to form two shorter dumbbells, to an analogous Brownian dynamics simulation of the same physical model. They found deficiencies in the VCM model and incorporated microscopic reversibility by extending an ensemble-averaged bead-spring phase space model to include reversible scission of two-spring chains; thus, they recover complete agreement with the BD results. They concluded that it would be important for future work to explore calculations with a FENE spring and with models with more than two species, and this observation reinforced our motivation to work with transient network models.

4.2. Effect of microstructural kinetics

Next, we explore the influence of the kinetic rate constants A and B on the evolution of microstates and their associated propensity to generate fluctuations in the velocity field even at low Reynolds numbers. We begin this study by determining the choice of kinetic rate constants, which through the process of microstructure breaking and recombination, lead to changes in flow. The set of values selected for the simulations in this section are: $\mathrm{Re} = 0.1$, $\mathrm{Wi} = 1$, $\beta(x, y, t = t_0) = 0.1$, $b = 50$ and $N_f = 2000$. The values of the kinetic constants and the Peclet number were determined using the material parameters in Table 3 which were taken from Fielding [31] and Varchanis et al. [32]. Accordingly, we have $A = 58$, $B = 27$, and $Pe = 1000$. The latter parameter can change substantially because it depends on the diffusive coefficient of the material.

Figure 6 shows the comparison of axial velocity and shear stress as a function of time by modifying the kinetic rate constants A and B. In Fig. 6a, the

Parameter	Symbol	Value	REF
Rheometer gap	L	0.15 mm	[33]
Density	ρ	10^3 kg m^{-3}	[33]
Solvent viscosity	η_s	10^{-3} kg m^{-1}s^{-1}	[33]
Polymeric viscosity	η_p	0.4 kg m^{-1}s^{-1}	[33]
Relaxation time	λ	3 s	[33]
Diffusion coefficient	D	3×10^{-11} m^{2}s^{-1}	[33]
Drag coefficient	ς	2.4×10^{12} kg m^{-3}s^{-1}	[33]
Kinetic generation constant	k^A	0.0058s^{-1}	[32]
Kinetic breakage constant	k^B	0.0017	[32]

Table 3: Material parameters of the model

velocity shows fluctuations, which are manifestations of the complex interactions between the microstates. These interactions also modify shear stress, as shown in Fig. 6b. Figure 7 shows the effect of increasing the magnitude of A and B by 50% and 100% for two values of the Peclet number, Pe $=$ 1000 and 3300, the same values used by Varchanis et al. [32]. The microstate concentrations in Fig. 7a show that as A and B increase, the interaction process between microstates becomes faster. This effect occurs at short times and generates fluctuations of the same order around the equilibrium concentration for both Pe numbers. The velocity and stress profiles exhibit the same behaviour when increasing the kinetic constants or modifying the Pe; however, when increasing the values of A and B, convergence is lost more quickly. This effect can be delayed by increasing the Peclet number to Pe=3300. This indicates that the diffusive effect stabilises the system, as shown in Figure 7. This effect was also found by [32]. It is important to mention that the values used for the kinetic constants were $A = 58$ and $B = 27$ for all subsequent simulations. With these values or lower, no convergence problems were found. Fig. 8 shows the evolution of the concentration distribution ω_1 and the superimposed velocity vectors, the latter not always completely parallel to the plates, indicating the fluctuations experienced by the velocity. The predictions in this section illustrate the complex interaction between the microstructures. In solutions of entanglement polymers and viscoelastic surfactants under shear, concentration fluctuations were first reported in experiments [34, 35], followed by theoretical studies developed by Helfand and Fredrickson [16, 36]. Hu and Lips [37], using the particle tracking velocimetry (PTV) technique, observed random fluctuations in the evolution of shear stress in an entangled micellar solution with shear banding.

4.3. Effect of viscosity ratio β

The viscosity ratio, β, is another important factor that contributes to the occurrence of fluctuations. Many models assume a constant value for β. However, in the transient network model studied in this paper, β is considered to be a function of the concentration of the microstructures, $\beta_0 = \beta_0(\omega_0, \omega_1)$. Since a viscosity is associated with each microstructure, an initial viscosity ratio $\beta_0 = \beta_0(x, y, t = t_0)$ is specified. The numerical simulations in this section were performed with the following parameter values: $Re = 0.1$, $\mathrm{Wi} = 1$, $A = 58$ and $B = 27$, $b = 50$ and $N_f = 2000$, for different initial values of the viscosity ratio ($\beta_0 = 1/3, 1/10, 1/13, 1/21$). As the value of β_0 decreases, the fluctuations in concentrations also decrease; however, the kinetic process is slightly faster, as shown in Fig. 9a and Fig. 9b. Regarding velocity and shear stress, the fluctuations and elastic overshoot that occur in the transient part decrease, as expected, since diluting the system approximates the behaviour of a viscous fluid (see Fig. 9c and Fig. 9d). The influence of the viscosity ratio on inestabilities has been reported by Zhou et al. [38] and Adams et al. [39], who suggested that there is a critical value of β for fluctations to manifest themselves. Fielding and Olmsted [33] studied the early stages of the instabilities using the non-local Johnson-Segalman model with a two-fluid coupling of flow to micellar concentration, and found a phase diagram that was qualitatively consistent with experiments on micellar solutions, with critical values for shear stress or strain rate and concentration.

4.4. Effect of extension length b

In the classical FENE model, the maximum extension length of the dumbbells b is constant. Although coupling FENE with the transient network model means that the dumbbell extension is variable, it never exceeds the maximum length of each microstructure (see Table 2). The numerical simulations in this section were performed using the following parameter values: $\mathrm{Re} = 0.1$, $\mathrm{Wi} = 1$, $A = 58$, $B = 27$, $\beta(x, y, t = t_0) = 1/10$ and $N_f = 2000$ for different maximum extension lengths $b = 10,\ 15,\ 30,\ 40,\ 50,\ 75$, and 100. Fig. 10 shows that the parameter b has no significant influence on the evolution of microstate concentrations or on the velocity profile (see Figs. 10a, b and Fig. 10c, respectively). Its main effect is on the shear stress, which increases as b decreases (see Fig. 10d. This means that microstates tend to behave like a rigid dumbbell, which undergoes small deformations. On the other hand, for small values of $b < 40$, the simulations present convergence problems, as shown in Fig. 10.

4.5. Influence of elasticity Wi

The numerical simulations in this subsection were performed with the following values: $\mathrm{Re} = 0.1$, $A = 58$, $B = 27$, $\beta(x, y, t = t_0) = 1/10$, $b = 50$ and $N_f = 2000$. Fig. 11 shows the influence of elasticity Wi on microstate concentrations, axial velocity, and shear stress. The evolution of microstate concentrations shows a higher frequency of fluctuation when $Wi = 0.5$ (see Fig. 11a and Fig. 11b). This indicates that the microstates experience a greater interaction between them. As elasticity increases, these fluctuations decrease, meaning that the system requires more energy for the microstates to interact, reducing the rate of the kinetic process. Furthermore, the average of both concentrations across the whole domain approaches 0.5 as Wi increases. Regarding the macroscopic response, the main indicator of changes in the elasticity of the system is the elastic overshoot that occurs in the transient part of the velocity profile, as shown in Figure 11c. After this, greater fluctuations in velocity are also observed for small values of Wi, which decrease as Wi increases. Miller and Rothstein [40] reported transient experiments, which were resolved at very short timescales and demonstrated the existence of a propagating damped elastic wave.

4.6. Effect of inertia (Re)

The numerical simulations in this section were performed with the following values: $\mathrm{Wi} = 1$, $A = 58$, $B = 27$, $\beta(x, y, t = t_0) = 1/10$, $b = 50$ and $N_f = 2000$. Fig. 12 shows the influence of inertia (Re) on microstate concentrations, axial velocity, and shear stress. Figs. 12a, b, and c show that as Re increases, concentrations take longer to reach equilibrium. Figs. 12d and 12e show a comparison between the velocity profile with and without fluctuations for two Reynolds numbers, $Re = 0.1$ and $Re = 1$. These figures show that as Re increases, the frequency of fluctuations decreases, but their amplitude increases, indicating that, with an appropriate value for the kinetic constants, Re contributes to the magnitude of the fluctuations, Fig. 12f, which for large values of Re can result in other phenomena such as shear banding or elastic turbulence. A similar effect is seen in the shear stress, as shown in Figs. 12g and 12h. As Re increases, an inertial overshoot is generated at the start-up of shear flow until equilibrium is reached, which is common in dynamic tests in rheology [9].

Quintero et al. [12] modelled and simulated active FENE bead–spring breaking/reforming single/double dumbbells in an imposed shear flow. They show that the shear stress converges to similar values, indicating a possible plateau, or even a negative slope in the flow curve for this range of shear rates. Fig. 13 shows the evolution of the concentration distribution ω_1 and the superimposed velocity vectors for $Re = 10$. In this figure, it can be seen that in the early stages, the diffusion of momentum in a direction perpendicular to the flow is coupled with the breakdown of the microstate ω_1, until the velocity acquires a linear profile starting from the bottom plate and the concentrations reach a equilibrium state with their respective fluctuations. Fig. 14 shows the evolution of the axial velocity and shear stress up to a time of $t = 24$ dimensionless units under the following conditions: $Re = 0.1$, $Wi = 1$, $A = 57$, $B = 28$, $\beta(x, y, t = t_0) = 1/10$, $b = 50$, $N_f = 2000$. This time interval is considered to evaluate the stability of the numerical code. This figure confirms that, once fluctuations in velocity and shear stress appear, they persist in time. Perge et al. [41] have shown that, even at vanishingly small Reynolds numbers, micellar surfactant solutions are model systems for studying shear band formation and elastic instabilities.

5. Conclusions

In this work, we investigated the interplay between microstructural kinetics and macroscopic flow behaviour in complex fluids using the FENE transient network model under simple shear flow. The main findings are summarized as follows:

- Microstructural breakage and recombination dynamics can generate persistent fluctuations in velocity and shear stress, even at vanishingly small Reynolds numbers, ruling out inertia as their sole origin.
- The viscosity ratio β, strongly influences the onset of fluctuations; dilution drives the system toward Newtonian-like behaviour with suppressed flow instabilities.
- The maximum extension length b of the dumbbells exerts limited influence on microstate concentrations and velocity but significantly affects shear stress, with small values of b contributing to increases in stress and numerical convergence challenges.
- The effect of elasticity Wi, modulates both microscopic and macroscopic responses: low elasticity promotes fluctuations, while high elasticity stabilizes the system.
- Inertia influences fluctuations whenever the rate of microstructural interaction exceeds a critical value.

The numerical predictions presented in this paper underscore the value of transient network models in bridging kinetic mechanisms with observable rheological responses. The FENE transient network model provides a predictive framework for analyzing flow instabilities in polymeric and micellar systems.

6. Acknowledgements

A. Mil-Martínez gratefully acknowledges the PhD scholarship of SECIHTI for financial support. R. O. Vargas would like to acknowledge the financial support IPN SIP-20253835, and the School of Mathematics of Cardiff University for the facilities provided during his sabbatical leave. L.M-S. acknowledges sabbatical support of the Secretaría de Ciencias, Humanidades, Tecnología e Innovación (SECIHTI). Juan P. Escandón thanks the sabbatical research program and the financial support of the grant number IPN SIP-20253830.

References

[1] J. Brannick, A. Kirshtein, C. Liu, Dynamics of Multi-Component Flows: Diffusive Interface Methods With Energetic Variational Approaches, in: Reference Module in Materials Science and Materials Engineering, Elsevier, 2016. doi:https://doi.org/10.1016/B978-0-12-803581-8.03624-9.

[2] R. G. Larson, The Structure and Rheology of Complex Fluids, Oxford University Press, 1999.

[3] S. M. Fielding, Complex dynamics of shear banded flows, Soft Matter 3 (2007) 1262–1279.

[4] S. Lerouge, Flow of wormlike micelles: From shear banding to elastic turbulence, Science Talks 3 (2022) 100050.

[5] M. S. Green, A. V. Tobolsky, A new approach to the theory of relaxing polymeric media., The Journal of Chemical Physics 14 (1946) 80 – 92.

[6] A. S. Lodge, A network theory of flow birefringence and stress in concentrated polymer solutions., Transactions of the Faraday Society 52 (1956) 120 – 130.

[7] A. Vaccaro, G. Marrucci, A model for the nonlinear rheology of associating polymers., Journal of Non-Newtonian Fluid Mechanics 92 (2000) 261–273.

[8] E. Rincón, A. Chávez, R. Herrera, O. Manero, Rheological modelling of complex fluids: A transient network model with microstates, Journal of Non-Newtonian Fluid Mechanics 131 (2005) 64 – 77.

[9] R. B. Bird, F. C. Curtiss, R. C. Amstrong, O. Hassager, Dynamics of Polymeric Liquids. Volume 2: Kinetic Theory, Second ed., 1987.

[10] O. Manero, J. E. Puig, F. Bautista, J. P. Garcia-Sandoval, Nonlinear viscoelasticity of complex fluids: A kinetic network model, Rheologica Acta 54 (2015) 53–67. doi:10.1007/s00397-014-0813-z.

[11] J. García-Sandoval, E. Hernandez, F. Bautista, , J. Puig, O. Manero, A simple kinetic model for complex rheological fluids based on irreversible thermodynamics, AIChE Journal 66 (2020) e16766.

[12] L. Quintero F., L. Zhou, L. Cook, Transiently linked nonlinear fene two species dynamics, Journal of Non-Newtonian Fluid Mechanics 301 (2022) 104720. doi:https://doi.org/10.1016/j.jnnfm.2021.104720.

[13] H. R. Warner, Kinetic theory and rheology of dilute suspensions of finitely extendible dumbbells, Industrial & Engineering Chemistry Fundamentals 11 (1972) 379–387.

[14] V. H. Ferrer, A. Gómez, J. A. Ortega, O. Manero, E. Rincón, F. López-Serrano, R. O. Vargas, Modeling of complex fluids using micro-macro approach with transient network dynamics, Rheologica Acta 56 (2017) 445–459.

[15] P. A. Vasquez, G. H. McKinley, L. P. Cook, A network scission model for wormlike micellar solutions: I. Model formulation and viscometric flow predictions, Journal of Non-Newtonian Fluid Mechanics 144 (2007) 122–139.

[16] J. D. Peterson, M. Cromer, G. H. Fredrickson, G. L. Leal, Shear banding predictions for the two-fluid Rolie-Poly model, Journal of Rheology 60 (2016) 927–951.

[17] N. Germann, L. P. Cook, A. N. Beris, Nonequilibrium thermodynamic modeling of the structure and rheology of concentrated wormlike micellar solutions, Journal of Non-Newtonian Fluid Mechanics 196 (2013) 51–57.

[18] A. A. Adams, M. J. Solomon, R. G. Larson, A nonlinear kinetic-rheology model for reversible scission and deformation of unentangled wormlike micelles, Journal of Rheology 62 (2018) 1419–1427.

[19] S. Lerouge, P. D. Olmsted, Non-local effects in shear banding of polymeric flows, Frontiers in Physics (2020) 246.

[20] A. Gómez-López, V. H. Ferrer, E. Rincón, J. P. Aguayo, A. E. Chávez, R. O. Vargas, Large-amplitude oscillatory shear flow simulation for a FENE fluid, Rheologica Acta 58 (2019) 241–260.

[21] R. O. Vargas, A. Gómez-López, J. P. Escandón, R. Mil-Martínez, T. N. Phillips, Multiscale modeling of complex fluids under SAOS and LAOS using a combined FENE transient network model, Physica Scripta 98 (2023) 025213.

[22] H. C. Öttinger, Stochastic Processes in Polymeric Fluids: Tools and Examples for Developing Simulation Algorithms, Springer, 1996.

[23] H. C. Öttinger, B. H. van den Brule, M. A. Hulsen, Brownian configuration fields and variance reduced CONNFFESSIT, Journal of Non-Newtonian Fluid Mechanics 70 (1997) 255–261.

[24] A. Lozinski, C. Chauviére, A fast solver for Fokker-Planck equation applied to viscoelastic flows calculations: 2D FENE model, Journal of Computational Physics 189 (2003) 607 – 625.

[25] A. Gómez-López, R. O. Vargas, A. Mil-Martínez, T. N. Phillips, Multiscale simulations of viscoelastic fluids in complex geometries using a finitely extensible nonlinear elastic transient network model, Physics of Fluids 36 (2024).

[26] J. F. Wendt, Computational Fluid Dynamics: An Introduction, Springer Science & Business Media, 2008.

[27] M. A. Hulsen, A. P. Van Heel, B. H. Van Den Brule, Simulation of viscoelastic flows using Brownian configuration fields, Journal of Non-Newtonian Fluid Mechanics (1997).

[28] T. N. Phillips, K. D. Smith, A spectral element approach to the simulation of viscoelastic flows using Brownian configuration fields, Journal of Non-Newtonian Fluid Mechanics 138 (2006) 98 – 110.

[29] R. O. Vargas, O. Manero, T. N. Phillips, Viscoelastic flow past confined objects using a micro–macro approach, Rheologica Acta 48 (2009) 373 – 395.

[30] A. Lozinski, R. G. Owens, T. N. Phillips, The Langevin and Fokker-Planck Equations in Polymer Rheology, in: R. Glowinski, J. Xu (Eds.), Numerical Methods for Non-Newtonian Fluids, volume 16 of *Handbook of Numerical Analysis*, Elsevier, 2011, pp. 211 – 303.

[31] S. M. Fielding, Linear instability of planar shear banded flow, Physical Review Letters 95 (2005) 134501.

[32] S. Varchanis, S. J. Haward, C. C. Hopkins, J. Tsamopoulos, A. Q. Shen, Evaluation of constitutive models for shear-banding wormlike micellar solutions in simple and complex flows, Journal of Non-Newtonian Fluid Mechanics 307 (2022) 104855.

[33] S. M. Fielding, P. D. Olmsted, Kinetics of the shear banding instability in startup flows, Physical Review E 68 (2003) 036313.

[34] O. Radulescu, P. Olmsted, J. Decruppe, S. Lerouge, J.-F. Berret, G. Porte, Time scales in shear banding of wormlike micelles, Europhysics Letters 62 (2003) 230–236.

[35] P. Fischer, E. K. Wheeler, G. G. Fuller, Shear-banding structure orientated in the vorticity direction observed for equimolar micellar solution, Rheologica Acta 41 (2002) 35–44.

[36] M.-A. Fardin, O. Radulescu, A. Morozov, O. Cardoso, J. Browaeys, S. Lerouge, Stress diffusion in shear banding wormlike micelles, Journal of Rheology 59 (2015) 1335–1362.

[37] Y. T. Hu, A. Lips, Kinetics and mechanism of shear banding in an entangled micellar solution, Journal of Rheology 49 (2005) 1001–1027.

[38] L. Zhou, P. A. Vasquez, L. P. Cook, G. H. McKinley, Modeling the inhomogeneous response and formation of shear bands in steady and transient flows of entangled liquids, Journal of Rheology 52 (2008) 591–623.

[39] J. Adams, S. M. Fielding, P. D. Olmsted, Transient shear banding in entangled polymers: A study using the Rolie-Poly model, Journal of Rheology 55 (2011) 1007–1032.

[40] E. Miller, J. P. Rothstein, Transient evolution of shear-banding wormlike micellar solutions, Journal of Non-Newtonian Fluid Mechanics 143 (2007) 22–37.

[41] C. Perge, M.-A. Fardin, S. Manneville, Surfactant micelles: Model systems for flow instabilities of complex fluids, European Physical Journal E 37 (2014) 1–12.

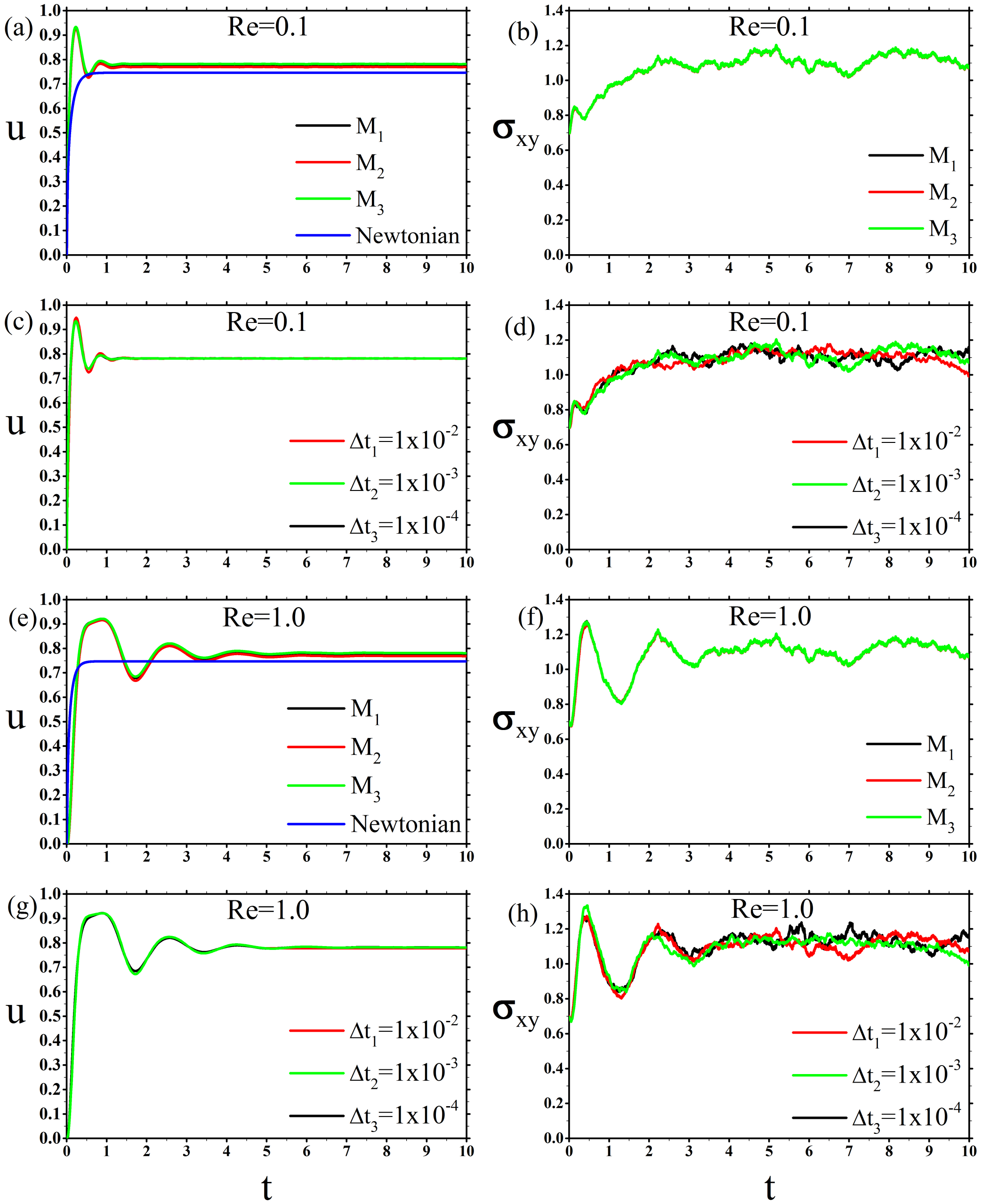

Figure 3: Mesh convergence of the evolution of the axial velocity component and shear stress at $(x, y) = (5, 0.75)$; for a structured network with Wi=1, $\beta = 1/10$, $A = 1$, $B = 1$, $b = 50$, $N_f = 2000$, for (a) Re = 0.1 and (b) Re = 1.

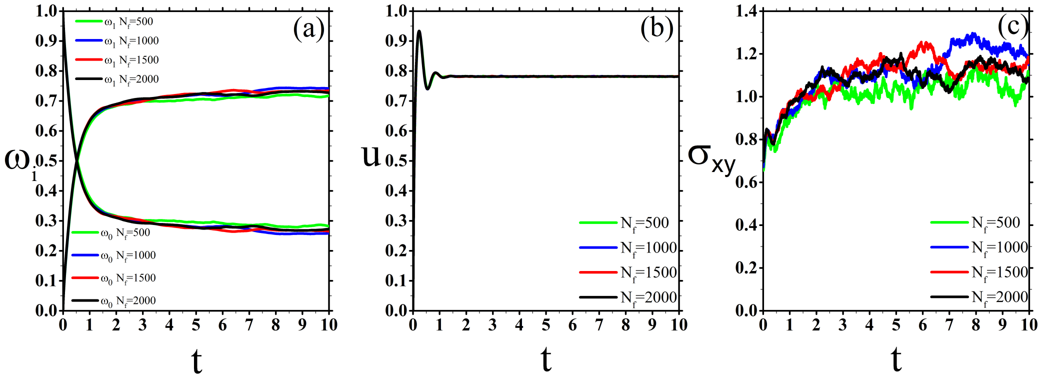

Figure 4: Effect of N_f on (a) the time evolution of the averaged microstate concentrations over the entire computational domain, (b) the axial velocity component, and (c) the shear stress for a structured network with: Re = 0.1, Wi = 1, $\beta = 1/10$, $b = 50$, $N_f = 2000$ at $(x, y) = (5, 0.75)$.

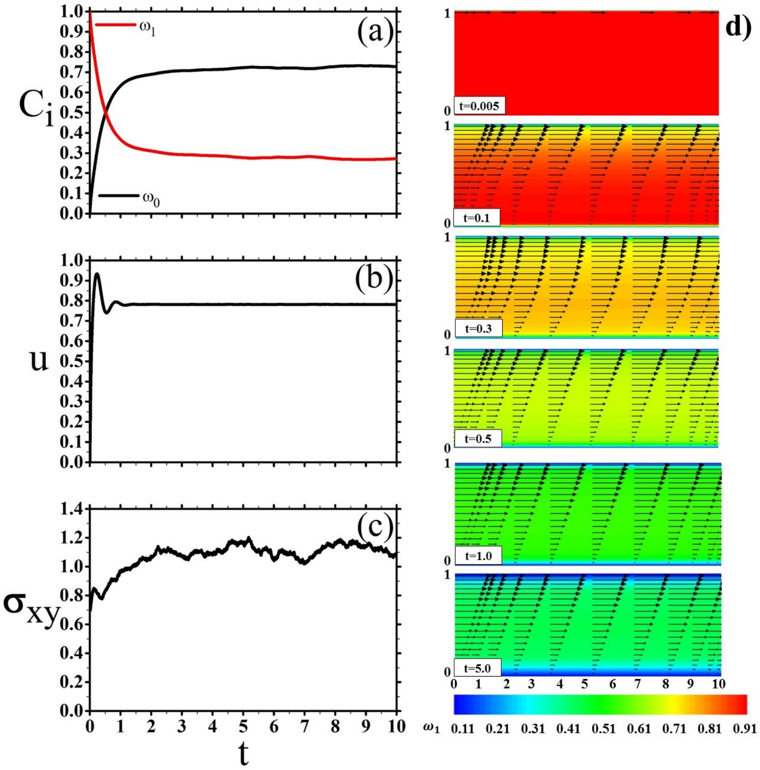

Figure 5: Evolution of (a) the average microstate concentrations over the computational domain; (b) axial velocity component at $(x, y) = (5, 0.75)$; (c) shear stress at $(x, y) = (5, 0.75)$; snapshots in time of (d) concentration distribution of ω_1 (contours) and velocity profiles (vectors), for a structured network with Re = 0.1, Wi = 1, $\beta_0 = 1/10$, $A = 1$, $B = 1$, $b = 50$, $N_f = 2000$.

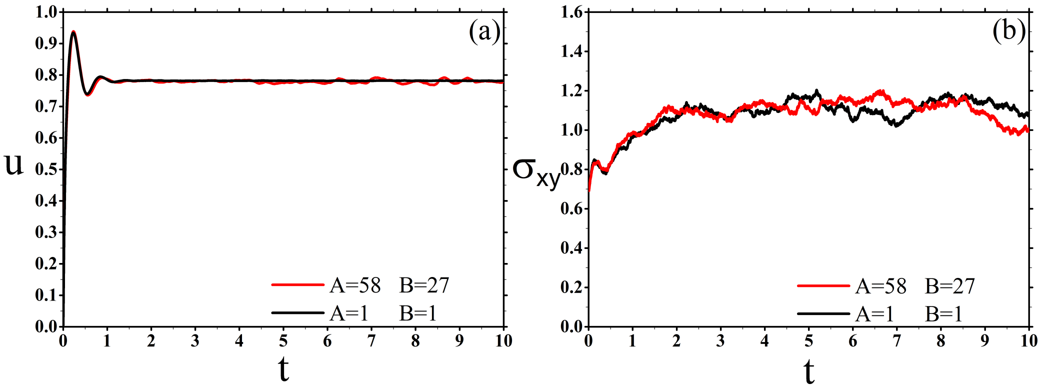

Figure 6: (a) Axial velocity component, and (b) shear stress at $(x, y) = (5, 0.75)$ with and without fluctuations for different values of kinetic rate constant A and B, with $\mathrm{Re} = 0.1$, $\mathrm{Wi} = 1$, $\beta(x, y, t = t_0) = 1/10$, $b = 50$, $N_f = 2000$, and $Pe = 1000$.

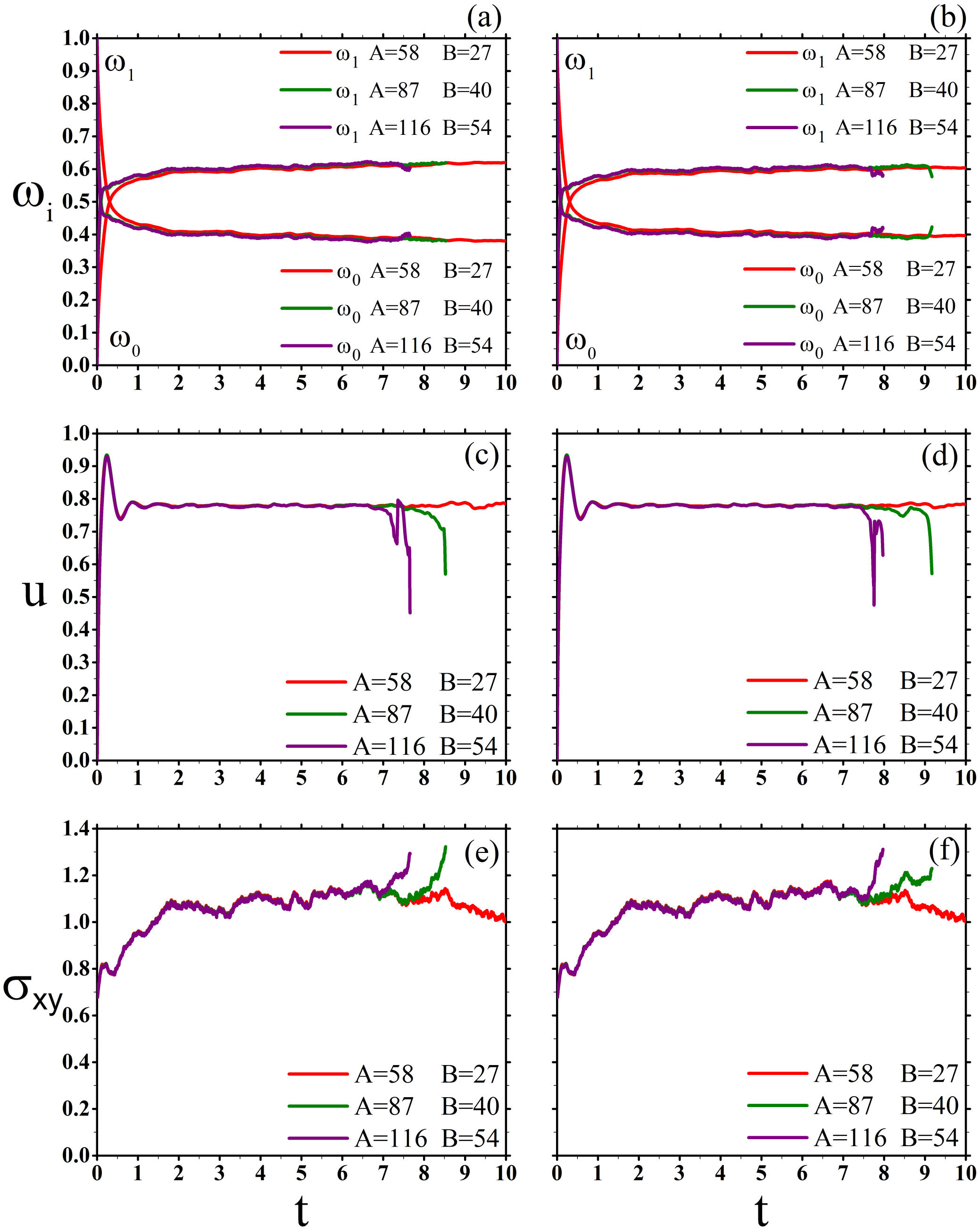

Figure 7: From top to bottom, evolution of the averaged microstate concentrations, axial velocity component, and shear stress at $(x, y) = (5, 0.75)$ for different values of kinetic rate constant A and B, $\mathrm{Re} = 0.1$, $\mathrm{Wi} = 1$, $\beta(x, y, t = t_0) = 1/10$, $b = 50$, and $N_f = 2000$. $Pe = 1000$ (a, c, e) and $Pe = 3300$ (b, d, f).

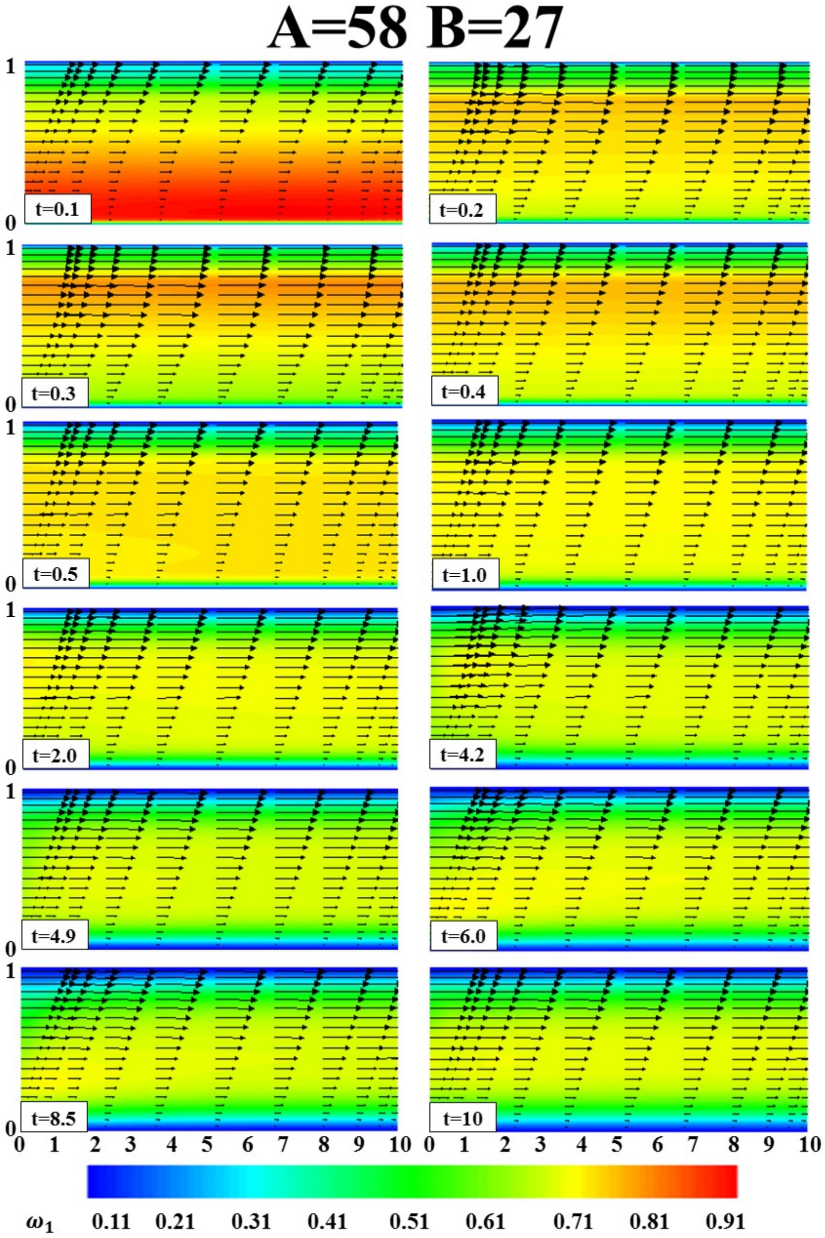

Figure 8: Evolution of concentration distribution ω_1 (contours) and velocity profiles (vectors), for a structured network with: $\mathrm{Re} = 0.1$, $\mathrm{Wi} = 1$, $\beta_0 = 1/10$, $A = 58$, $B = 27$, $b = 50$, $N_f = 2000$, and $Pe = 1000$ throughout the computational domain.

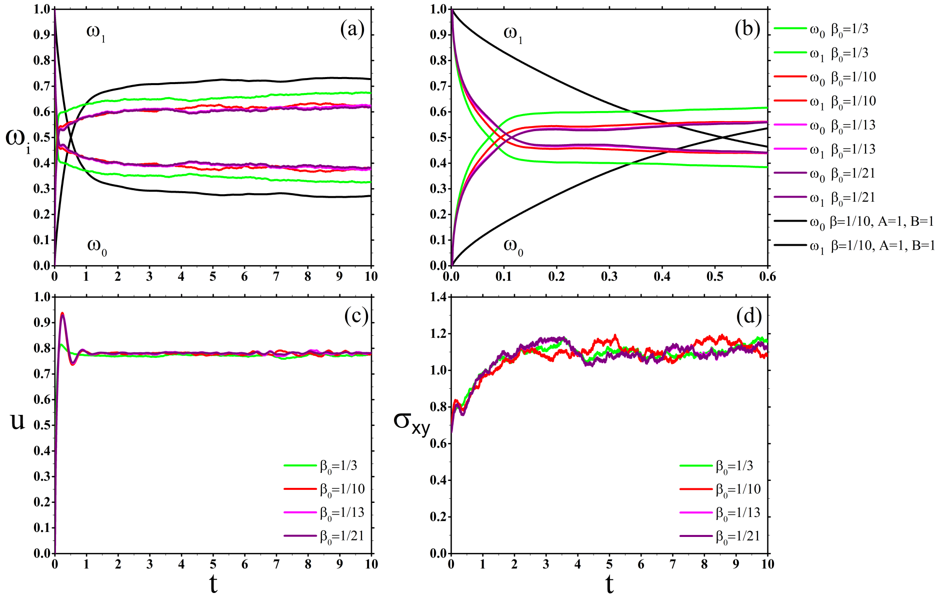

Figure 9: Evolution of the averaged microstate concentrations (a) $t \in [0, 10]$; (b) $t \in [0, 0.6]$; axial velocity component (c), and shear stress (d) at $(x, y) = (5, 0.75)$, for different values of initial viscosity ratio β_0, with $\mathrm{Re} = 0.1$, $\mathrm{Wi} = 1$, $b = 50$, $N_f = 2000$, and $Pe = 1000$.

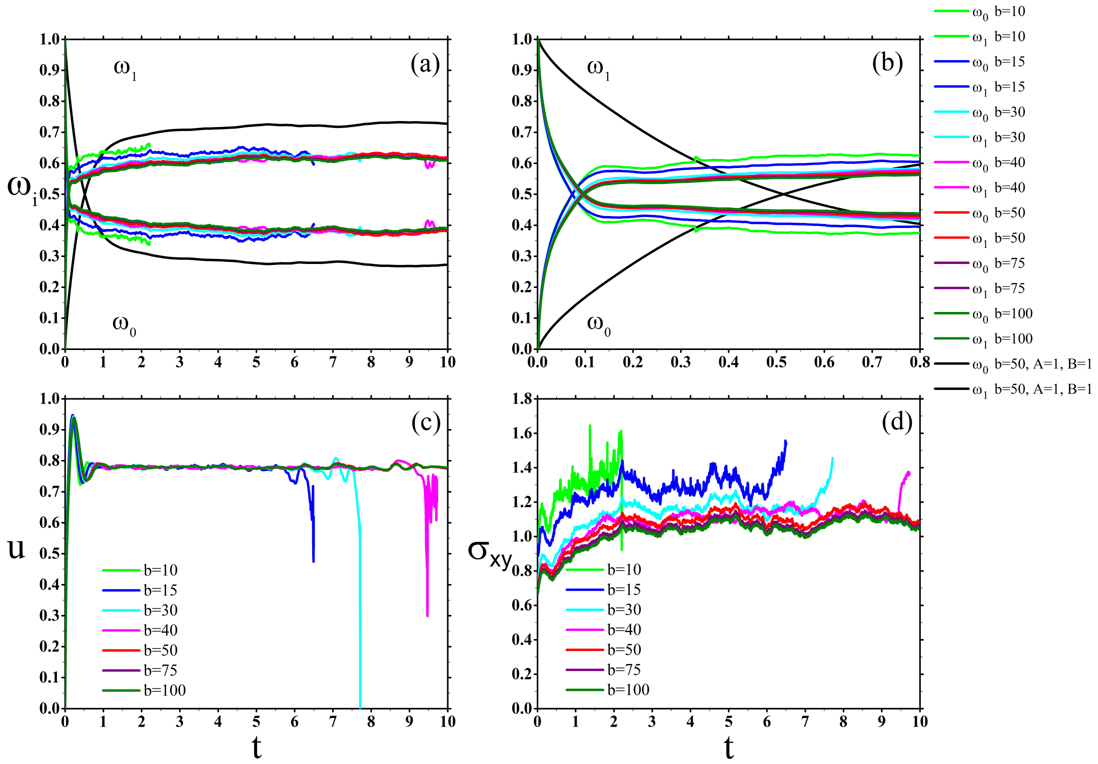

Figure 10: Evolution of the averaged microstate concentrations (a) over $[0, 10]$; (b) over $[0, 0.8]$; axial velocity component (c), and shear stress (d) at $(x, y) = (5, 0.75)$ for different values of extension length b. With $A = 58$ and $B = 27$, Re $= 0.1$, Wi $= 1$, $\beta(x, y, t = t_0) = 1/10$, $N_f = 2000$, and $Pe = 1000$.

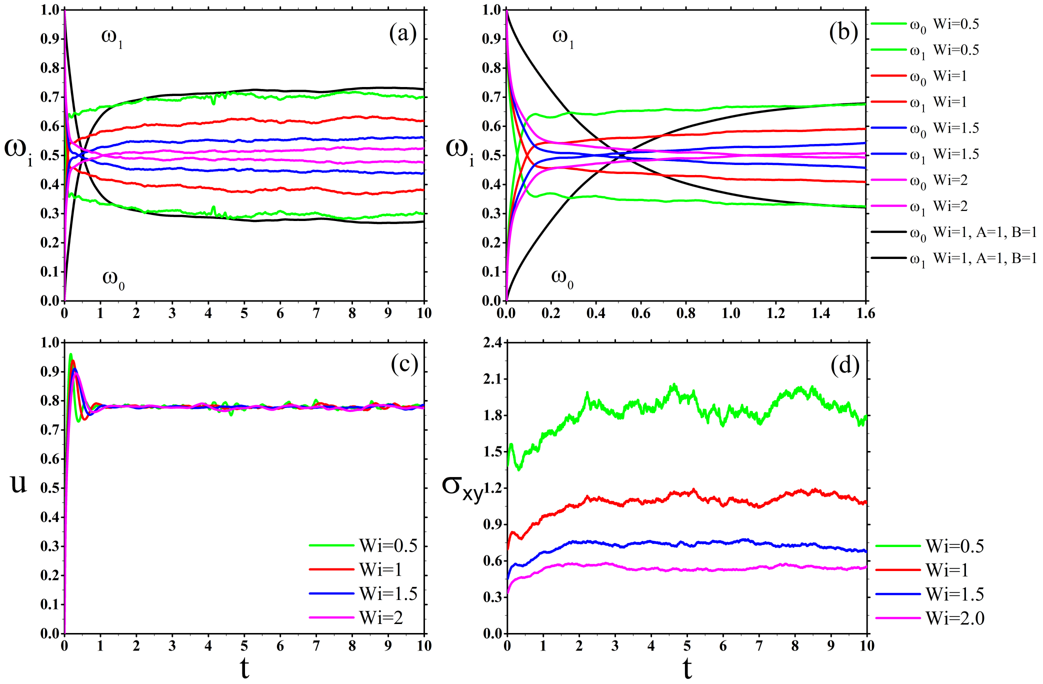

Figure 11: Evolution of the averaged microstate concentrations (a) over $[0, 10]$; (b) over $[0, 1.6]$; axial velocity component (c), and shear stress (d) at $(x, y) = (5, 0.75)$ for different values of Weissenberg number Wi, with $\text{Re} = 0.1$, $\beta(x, y, t = t_0) = 1/10$, $b = 50$, $N_f = 2000$, and $Pe = 1000$.

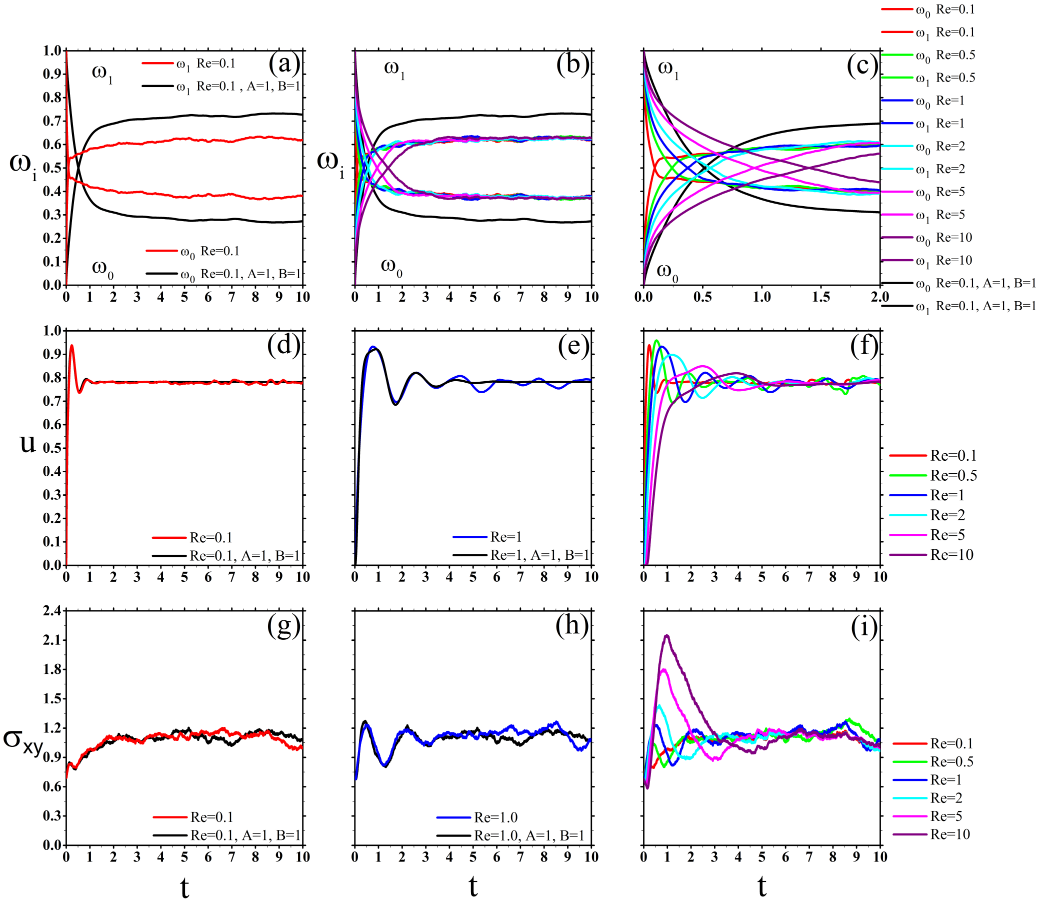

Figure 12: Evolution of the averaged microstate concentrations (a) and (b) over $[0, 10]$; (c) over $[0, 2.0]$; axial velocity component (d-f), and shear stress (g-i) at $(x, y) = (5, 0.75)$ for different values of Reynolds number Re, with $\mathrm{Wi} = 1$, $\beta(x, y, t = t_0) = 1/10$, $b = 50$, $N_f = 2000$, and $Pe = 1000$.

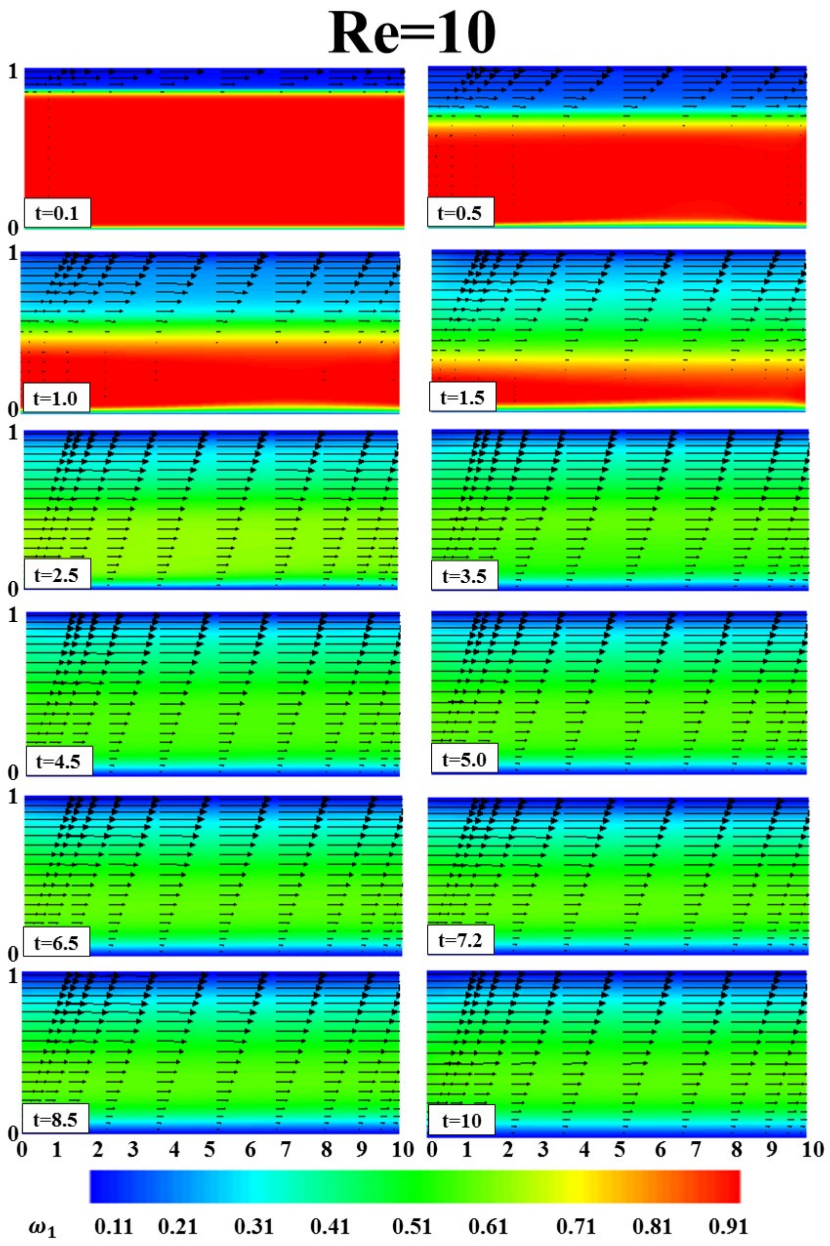

Figure 13: Evolution of concentration distribution of ω_1 (contours) and velocity profiles (vectors), for a structured network with: $\mathrm{Re} = 0.1$, $\mathrm{Wi} = 1$, $A = 58$, $B = 27$, $\beta_0 = 1/10$, $b = 50$, $N_f = 2000$, $Pe = 1000$ throughout the computational domain.

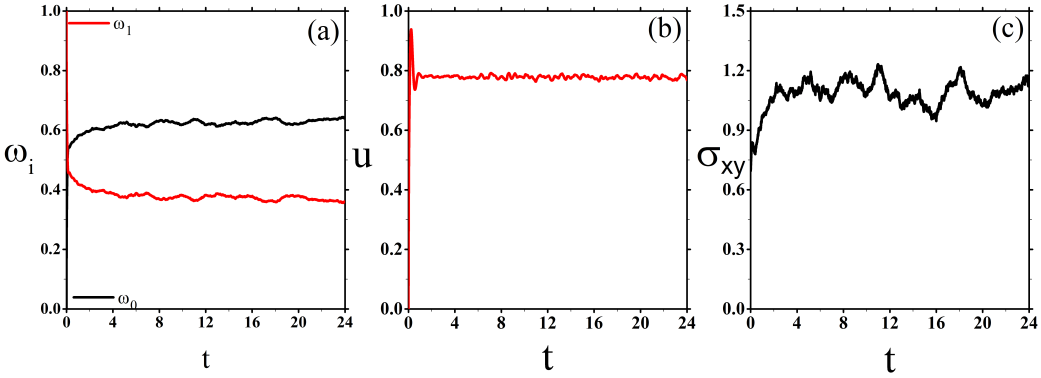

Figure 14: Effect of the long times evolution of (a) averaged microstate concentrations,(b) axial velocity component, and (c) shear stress at $(x, y) = (5, 0.75)$ for a structured network with: $\mathrm{Re} = 0.1$, $\mathrm{Wi} = 1$, $A = 58$, $B = 27$, $\beta_0 = 1/10$, $b = 50$, $N_f = 2000$, and $Pe = 1000$.